Climate Dynamics (2019) 53:4019–4035
https://doi.org/10.1007/s00382-019-04768-3

A climatology of daily synoptic circulation patterns and associated surface meteorology over southern South America

Paul C. Loikith[1] · Luana Albertani Pampuch[2] · Emily Slinskey[1] · Judah Detzer[1] · Carlos R. Mechoso[3] · Armineh Barkhordarian[4]

Received: 5 January 2019 / Accepted: 9 April 2019 / Published online: 16 April 2019

Abstract
Synoptic circulation patterns, defined as anomalies in sea level pressure (SLP), 500 hPa geopotential height (Z500), and 250 hPa wind speed (V250) and referred to as large-scale meteorological patterns (LSMPs), are characterized using the self-organizing maps approach over southern South America. Results show a wide range of possible LSMP types over a 37-year period of study. LSMP type variability can be summarized as a spectrum from patterns dominated by positive SLP and Z500 anomalies with a poleward displacement of the strongest 250 hPa winds, to patterns dominated by similar structures but with anomalies of opposite sign. The LSMPs found are connected with lower tropospheric temperature and wind, precipitation, and the frequency of atmospheric rivers (ARs). This highlights LSMPs more closely associated with anomalous and potentially impactful surface meteorology. Results show ARs as primary drivers of heavy precipitation over some of the region and connect their occurrence to driving synoptic dynamics. Two important low frequency modes of climate variability, the Southern Annular Mode (SAM) and the El Nino Southern Oscillation (ENSO), show some influence on the frequency of LSMP type, with the SAM more directly related to LSMP type modulation than ENSO. This comprehensive climatology of synoptic variability across southern South America has potential to aid in a mechanistic approach to studying climate change projections of temperature, precipitation, and AR frequency in climate models.

Keywords Synoptic climatology · South America · Atmospheric rivers

1 Introduction

Synoptic scale atmospheric circulation patterns are important drivers of weather and climate over midlatitude regions. These patterns, often referred to as large-scale meteorological patterns (LSMPs), are associated with several processes key for local to regional scale surface weather and climate variability including horizontal temperature advection, promotion or inhibition of precipitation, and important thermodynamic processes such as radiational cooling or warming due to subsidence. LSMPs are further associated with extreme weather and climate. For example, multiple studies have documented the LSMPs associated with extreme temperature events across a wide range of geographies (e.g. Grotjahn et al. 2016; Loikith and Broccoli 2012; Krueger et al. 2015; Chen and Lu 2016; Xie et al. 2017; Cassano et al. 2016; Pezza et al. 2012; Renom et al. 2011; Geirinhas et al. 2018). Similarly, LSMPs have been connected with extreme precipitation events (e.g. DeAngeles et al. 2013; Kawazoe and Gutowski 2013). A comprehensive understanding of LSMP climatology and connections between patterns and surface meteorology is important for understanding the range of weather and climate dynamics for a region, which in turn can provide a basis for understanding mechanisms behind climate trends and projections of future change. Furthermore, LSMPs can provide a target for climate model evaluation, informing on the dynamical reasons for model bias and boosting confidence in model skill

✉ Paul C. Loikith
ploikith@pdx.edu

[1] Department of Geography, Portland State University, Portland, OR, USA

[2] Departamento de Engenharia Ambiental, Instituto de Ciência e Tecnologia, UNESP-Univ. Estadual Paulista, Campus São José dos Campos, São José dos Campos, SP, Brazil

[3] Department of Atmospheric and Oceanic Sciences, University of California Los Angeles, Los Angeles, CA, USA

[4] Jet Propulsion Laboratory, California Institute of Technology, Pasadena CA, USA

when realistically simulated (Loikith et al. 2015; Loikith and Broccoli 2015; Grotjahn and Lee 2016).

Despite the importance of understanding LSMPs and their associated meteorological impacts, relatively few studies have highlighted the range of LSMPs that occur over southern South America. Solman and Menendez (2003) used cluster analysis to define five weather regimes in daily 500 hPa geopotential height field over southern South America and adjacent oceans and connected the regimes to surface temperature anomalies. Using k-means clustering, Muñoz et al. (2015) identified six weather types based on 850 hPa geopotential height anomalies and connected them to extreme precipitation over southeastern South America, focusing on the South Atlantic convergence zone region.

Other studies involving large-scale atmospheric circulation over southern South America have examined the relationship between low-frequency modes of climate variability and higher frequency LSMPs and surface meteorology. For example, the Southern Annular Mode (SAM; Thompson and Wallace 2000) has been demonstrated as influential on near surface temperature variability over the region with positive phases of the SAM associated with warm anomalies and negative phases with cold anomalies (Silvestri and Vera 2009; Loikith et al. 2017b; Gillett et al. 2006; Garreaud et al. 2009). Defined as anomalies in atmospheric mass between the Antarctic and mid-latitudes, the SAM can influence LSMP type and frequency at the synoptic scale. While the El Niño Southern Oscillation (ENSO) is generally more associated with climate impacts equatorward of extratropical South America (e.g. Andreoli and Kayano 2005; Grimm and Tedeschi 2009; Kayano et al. 2017), there is evidence of remote teleconnections influencing precipitation and temperature variability, especially at the seasonal scale, over portions of the region (Grimm et al. 2000; Garreaud et al. 2009).

One challenge in studying LSMPs is the inherent size and variability of the data to be analyzed. For example, when focusing on a single location, one can identify features of interest such as heatwaves and the associated LSMPs (e.g. Krueger et al. 2015; Lee and Gotjahn 2016; Lau and Nath 2012). Diagnosing the synoptic drivers of the heatwave would likely require assessing LSMPs across multiple variables at multiple levels in the atmosphere, often using composite analysis. These variables may include, for example, sea level pressure (SLP), wind, and geopotential height. Furthermore, the LSMPs associated with heatwaves at adjacent locations likely differ from those at the single location, complicating analysis if one were interested in the LSMPs associated with heatwaves across a region. Several approaches have been employed to reduce the complexity of studying LSMPs associated with meteorological impacts across a region, often involving some form of clustering, such as k-means (e.g. Muñoz et al. 2015), self-organizing maps (SOMs; e.g. Loikith et al. 2017a; Lennard and Hegerl 2015; Cassano et al. 2015) or empirical orthogonal function analysis (EOF; e.g. Lau and Nath 2012).

Here we present a comprehensive climatology of daily LSMPs over southern South America and connect synoptic scale atmospheric circulation patterns with lower tropospheric temperature and wind, and precipitation. We also look at column integrated water vapor transport and atmospheric rivers (ARs), as ARs have been shown to be commonly occurring across portions of this region and are known globally as key mechanisms for heavy precipitation (Waliser and Guan 2017), using SOMs as the basis for characterizing the range of LSMPs. We further assess whether and to what extent the SAM and ENSO provide background conditions that preferentially favor certain types of LSMPs over others to better explain the influence of low frequency modes of climate variability on daily synoptic climatology.

2 Data and methodology

2.1 Data

We use daily SLP, 500 hPa geopotential height (Z500), 250 hPa wind speed (V250), 850 hPa air temperature (T850), 850 hPa wind speed and direction (V850), column integrated water vapor transport (IVT), and precipitation data from the Modern Era Retrospective-Analysis for Research and Applications version 2 (MERRA2) reanalysis over the 37-year period of 1980–2016 for this study. MERRA2 is the latest generation of atmospheric reanalysis products from the United States (U.S.) National Aeronautics and Space Administration and is provided on a 0.5° latitude by 0.625° longitude grid at hourly temporal resolution. Data are freely available via the web (Gelaro et al. 2017; https://gmao.gsfc.nasa.gov/reanalysis/MERRA/). Precipitation data from MERRA2 are from the available bias corrected precipitation variable. While reanalysis precipitation can be associated with uncertainty, MERRA2 precipitation has shown some improvement over previous iterations (Reichle et al. 2018) and suffices for our goals of broadly connecting precipitation patterns with LSMPs.

Index values for ENSO and SAM are obtained from the U.S. National Oceanic and Atmospheric Administration's Earth System Research Laboratory (https://www.esrl.noaa.gov/psd/data/climateindices/list/). The Multivariate ENSO Index (MEI) is a bimonthly index based on six key ENSO-related variables centered over the tropical Pacific (Wolter and Timlin 1998). Negative values of the MEI relate to La Niña conditions, while positive MEI values relate to El Niño conditions. Here, we refer to the second of the 2 months of the bimonthly index such that a January value represents the December–January index value centered between the

2 months. Each day is assigned the MEI bi-monthly value for the month in which the day resides. The SAM index values are provided daily.

2.2 Methodology

2.2.1 Self-organizing maps

Large-scale meteorological patterns are characterized using the SOMs approach. SOMs are a class of unsupervised neural networks that organize input data (daily LSMPs in this case) into a user-selected set of output nodes (Sheridan and Lee 2011). We provide daily fields of SLP, Z500, and V250 simultaneously as input. The SOMs approach has been demonstrated as an effective tool in synoptic meteorology and climatology (e.g. Hewitson and Crane 2002; Johnson et al. 2008; Johnson and Feldstein 2010; Glisan et al. 2016) at identifying key LSMPs and connecting them with important meteorological events such as temperature and precipitation extremes (Gibson et al. 2017; Loikith et al. 2017a, b; Cassano et al. 2015, 2016; Ford and Schoof 2016). SOMs have also been used to study other large-scale meteorological phenomena such ARs (Radic et al. 2015), sea ice variability (Chen et al. 2016), and patterns of Arctic airmasses under Arctic amplification (Gervais et al. 2016).

As used in this study, the patterns associated with SOM output nodes represent a range or continuum of LSMPs with each day in the input record assigned to the node it shares the most similarities with. The SOMs routine begins by seeding a user-defined number of nodes with input data (daily LSMPs of SLP, Z500, and V250 provided simultaneously as input in this study). Next, the first input data point (in this case the tri-variate LSMP for the first day in the record) is assigned to the node with the smallest Euclidean distance between the input data and the seeded node. This "winning" node is then adjusted closer to the input data as are the surrounding nodes with the distance of adjustment from the winning node being determined by the user-defined neighborhood radius. This process is repeated for each data point numerous times until the SOM is stable (here we use an initial training length of 100 and 300 iterations for finetuning). The result is a matrix spanning the range of synoptic patterns with each day in the input climatology assigned to a node. While the result has some commonalities to other well-established methodologies such as k-means clustering, one advantage to the use of SOMs in the study of synoptic climatology is the ability to capture a continuum of patterns including patterns that would not necessarily be well-captured in cluster analysis because they would fall in between clusters (Lennard and Hegerl 2015).

The first step in applying the SOMs approach is to choose the number of output nodes of the SOM. This is usually performed with some level of subjectivity, balancing the need to capture a sufficient level of detail in the range of possible output patterns (i.e. the LSMPs) while not having so many patterns that results are difficult to interpret physically. In this sense, a larger SOM would provide a more detailed set of node patterns with fewer days assigned to each node while a smaller SOM would provide a more generalized set of patterns. An optimal number of nodes should result in a SOM that captures the range of possible LSMP types with node patterns in one corner of the SOM most different from the patterns in the opposite corner of the SOM. In this study, we found that a 35-node SOM in a 7×5 rectangular matrix using an initial training radius of five, met these optimal criteria after assessing results using smaller and larger SOMs.

Following Loikith et al. (2017a, b), we provide three atmospheric circulation variables as input to the SOM simultaneously. The input data is provided over the domain bounded on the north and south by $-34°$ and $-57.5°$ north latitude respectively and on the east and west by $-50°$ and $-90°$ east longitude respectively. Anomalies in SLP, Z500, and V250 are provided as input to capture information on near surface, mid-troposphere, and upper troposphere circulation respectively. This allows the SOM to be trained using more complete information about the synoptic state of the atmosphere than if only one variable were used. Anomalies of all variables are computed by subtracting the daily mean climatology from each day. Prior to the SOM construction, these anomalies are normalized by their temporal standard deviation to reduce the potential disproportionate influence of one quantity. Next, all input data were weighted by the square root of the cosine of latitude to account for area differences across the grid cells. These normalizations were then removed after the SOM was constructed so that results are displayed as anomalies. A single SOM is constructed for the entire dataset, as opposed to performing the SOM analysis on each season separately, for reasons justified below.

2.2.2 Atmospheric river identification

ARs are broadly defined as long, narrow corridors of high values of integrated water vapor transport (IVT; Zhu and Newell 1998). They are a common meteorological feature over southern South America and are an important mechanism for heavy precipitation especially along the Pacific Coast (Viale et al. 2018; Waliser and Guan 2017; Gimeno et al. 2016). To identify days with an AR at each grid point, we employ an objective identification algorithm based on the one introduced in Guan and Waliser (2015). The first step in this approach is to identify contiguous regions (i.e. areas of connected grid cells), or "objects", where the IVT values exceed the 85th percentile of the IVT climatology. Additional objects are identified within the spatial confines of the original object, using four additional thresholds at 2.5 percentile intervals ending at

the 95th percentile, following Lavers et al. (2012). This ensures that an AR that is embedded within an area of enhanced IVT that does not meet the additional geometric criteria of an AR is still captured. Percentiles are calculated relative to a 5-month IVT climatology, centered on the month of interest, specific to each grid cell and computed relative to the period of 1980–2016 (Guan et al. 2018).

Objects retained from the IVT thresholding exceedances are further filtered using directional and geometric requirements. IVT direction must not change more than 45° with respect to the mean IVT direction of the object and must be directed poleward. Geometric requirements further filter objects based on the object length, which is computed as the summation of the distances between neighboring grid cells along the AR axis or the maximum great circle distance between the opposites ends of the AR, and must exceed 2000 km (Ralph et al. 2004; Neiman et al. 2008). Furthermore, AR width is calculated as the ratio of the object's Earth surface area divided by its length and must exceed a value of two. If all of these criteria are met, an AR is identified, and all grid cells within the AR object are considered to have an AR day. IVT data are from MERRA2 reanalysis.

3 Results

3.1 Climatological overview

Figure 1 shows seasonal and annual mean climatologies for T850 and V850, the three circulation variables provided as input to the SOM, and precipitation over the region. The top row depicts the seasonal cycle in T850 and V850 over the region highlighting the predominance of the westerlies and an enhanced seasonal cycle in temperature in the north relative to the south where marine influence dampens the magnitude of seasonality. Seasonal variations in SLP and Z500 are relatively nuanced, but is possible to note the seasonal migration of the South Atlantic and Pacific subtropical highs, while the 250 hPa jet stream shows a more robust equatorward migration from DJF to

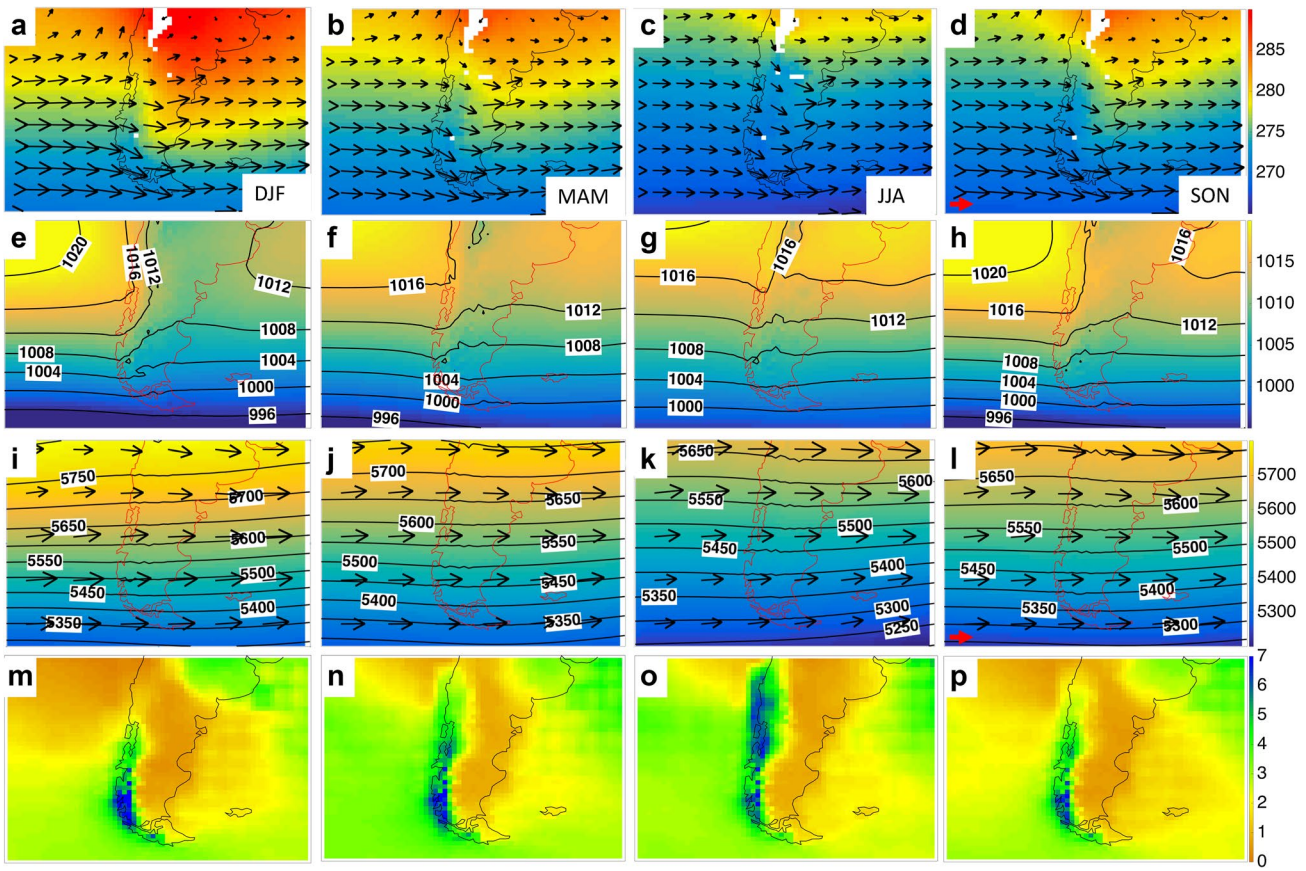

Fig. 1 37-Year averages of **a**–**d** 850 hPa temperature (shaded, in units of K) and wind (arrows, in units of m/s), **e**–**h** sea level pressure (in units if hPa), **i**–**l** 500 hPa geopotential height (shaded, in units of m) and 250 hPa wind (arrows, in units of m/s), and **m**–**p** precipitation (in units of mm/day). The columns are for different meteorological seasons starting at left DJF, MAM, JJA, and SON. The red arrow at the bottom left of **d** represents 10 m/s and the red arrow at the bottom left of **l** represents 20 m/s

JJA. Annual average precipitation (bottom row) is highest along the southern Pacific Coast, where the westerlies intercept the southern Andes Mountains, with relatively high amounts of precipitation extending farthest north in JJA. Regions in the lee of the Andes are consequently dry in all seasons, with the northeastern reaches of the domain also receiving substantial annual rainfall.

3.2 Large-scale meteorological patterns

The SOM for each of the three input variables is shown in Fig. 2. The 35 node SOM effectively displays the range of possible LSMPs with patterns in the corners generally opposite one another. For example, Node 29 at the lower left is dominated by anomalously high SLP, Z500, and anomalously weak V250, whereas Node 7 at the upper right is characterized by anomalously low SLP and Z500 with positive V250 anomalies over much of the domain. The SOM layout is oriented such that days with anomalously positive SLP and Z500 values combined with weak V250 winds and/or anomalously strong V250 winds along the southern edge are assigned to nodes towards the bottom left of the SOM. Days with the opposite pattern are assigned to nodes towards the top right, while days with a mix of positive and negative SLP and Z500 anomalies along with positive V250 anomalies centered over the domain are assigned to nodes in the middle of the SOM.

In building Fig. 2, all days from the entire annual cycle are provided as input to the SOM, as opposed to constructing a separate SOM for each season. This choice was made because the seasonal cycle in the three quantities, especially SLP and Z500, is relatively modest (Fig. 1) and allows the SOM to be trained over the largest possible set of data. Furthermore, the anomalies have the seasonal cycle removed prior to being provided as input to the SOM. However, some nodes occur preferentially during some months or seasons. Each bar in the 12-bar histograms in Fig. 3 gives the relative occurrence of the corresponding node for the month, starting with January at the left and ending with December at the right and color coded by meteorological season (red for summer, cyan for autumn, blue for winter, and green for spring). For example, Nodes 15, 21, 22, and 28 preferentially occur during the cooler months and Nodes 5, 9, 16 and 26 occur more frequently during warmer months. No nodes are strongly associated with the shoulder seasons alone. Additionally, Fig. 3 shows the number of days in the entire 37-year period assigned to each node. While no node(s) stand out as especially common or uncommon, Nodes 5, 6, and 33 have a relatively large number of days assigned to them while Nodes 14, 21, 30 and 31 show a relative minimum in assignments.

3.3 Meteorological associations

Since each day in the 37-year period is assigned to one of the 35 nodes, it is straightforward to construct composites of other meteorological variables that are related to the three SOM input quantities. Figure 4 shows composites of T850 and T850 anomalies for all days assigned to each node to help diagnose how the SOM defined LSMPs connect with low-level meteorology. Additionally, V850 vectors are overlaid on the T850 values. Here we refer to the T850 and V850 patterns by the node number they are associated with. Note that we use 850 hPa instead of 2-m and 10-m temperature and wind, respectively, because surface quantities are not directly assimilated into MERRA2. Some general patterns emerge in Fig. 4. First, the nodes at the bottom left show positive T850 anomalies in the southern and western portion of the domain. As one moves from bottom left to top right, this area of positive anomalies moves from southwest to northeast while an area of negative anomalies retreats to the northeast and another follows the warm anomalies from the southwest.

Including anomaly winds in the maps in Fig. 4 clearly captures that T850 anomalies are primarily associated with horizontal temperature advection driven by low level circulation anomalies. More specifically, regions of positive temperature anomalies coincide with V850 from the north (as is apparent for Nodes 19, 20, 25, 26, 30 and 31) while cold anomalies coincide with V850 more from the south (as for Nodes 2, 3, 6, 8, 15, and 22). Relatively small temperature anomalies (as for Nodes 4, 5, and 12) coincide with V850 that closely resembles the climatology in Fig. 1.

The LSMPs provided by the SOM in Fig. 2 can help diagnose the meteorological mechanisms driving the T850 anomalies in Fig. 4. For example, for Node 25 much of the domain exhibits positive temperature anomalies coincident with V850 exhibiting a northerly component. These winds blow across the climatological temperature gradient, transporting warmer air poleward as evident not only in the positive temperature anomalies in Fig. 4, but also the southeastward bulge in the T850 isotherms. A strong SLP anomaly gradient in the Node 25 SLP pattern in Fig. 2 results from a positive SLP anomaly to the east and a negative anomaly to the west. This difference in pressure promotes the northerly V850 component leading to low-level warm air advection. This also coincides with a Z500 ridge and upstream Z500 trough and anomalously strong V250 along the southern portion of the domain, indicative of a poleward displacement of the jet stream and a warm airmass.

Node 15, on the other hand, shows notable cold T850 anomalies over the entire land area of the domain along with V850 from the south and southwest. The T850 cold anomalies are maximized in the vicinity of Bahía Blanca, Argentina, where the angle between 850 hPa wind vectors and the

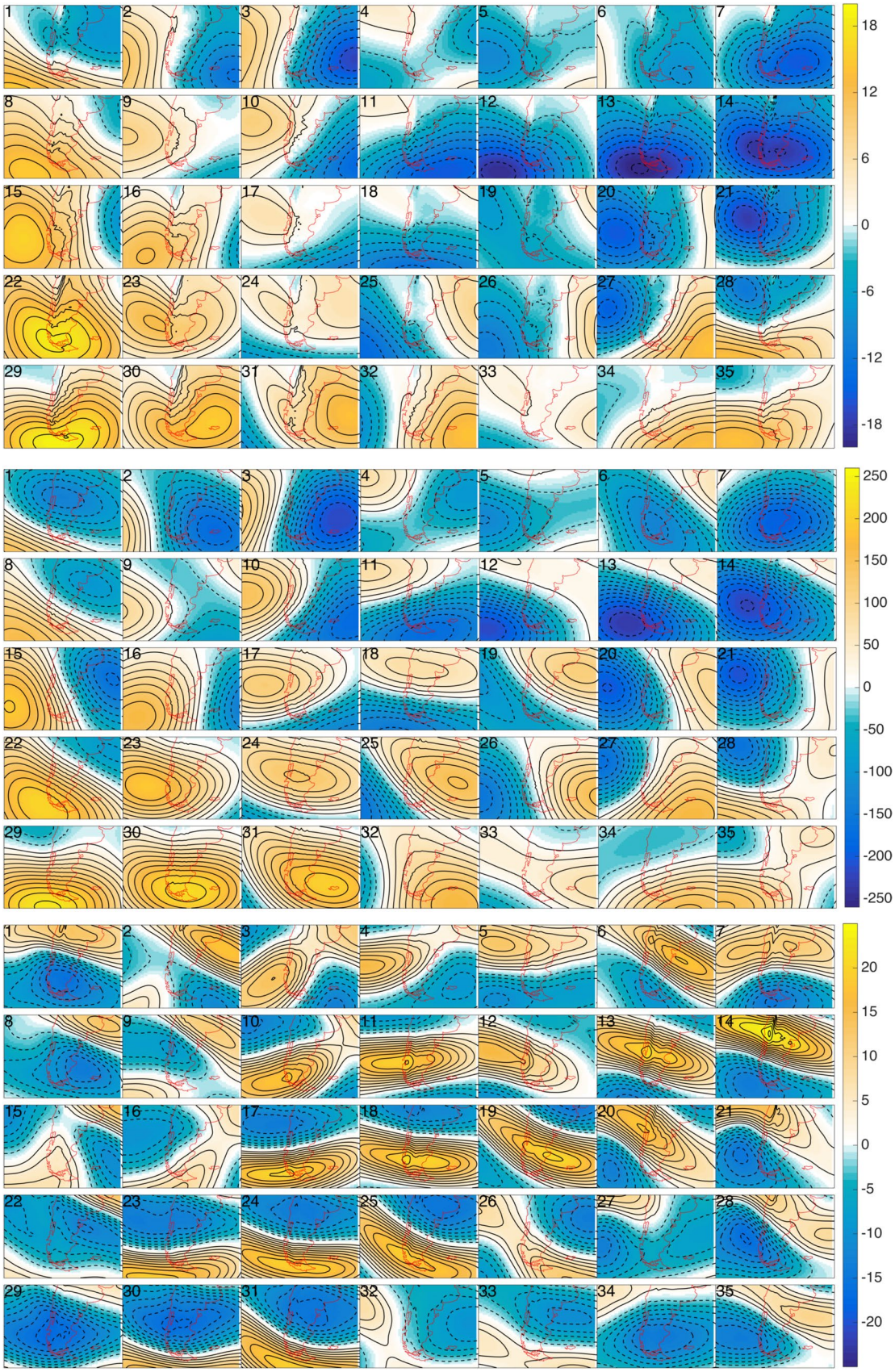
1
2
3
4
5
6
7
8
9
10
11
12
13
14
15
16
17
18
19
20
21
22
23
24
25
26
27
28
29
30
31
32
33
34
35
18
12
6
0
-6
-12
-18
250
200
150
100
50
0
-50
-100
-150
-200
-250
20
15
10
5
0
-5
-10
-15
-20

◂**Fig. 2** The self-organizing maps results for all days in the 37-year period. The top set of 35 panels are for SLP anomalies (in hPa), the middle for Z500 anomalies (in m), and the bottom for V250 (in m/s). The numbers in the upper left of each panel are the node numbers referenced in the text

T850 isotherms are most orthogonal. The SLP anomaly pattern for Node 15 clearly diagnoses the dynamic mechanism behind this low level circulation leading to the cold anomalies. The anomalous pressure gradient arising from the positive and negative anomalies to the west and east respectively promotes flow from the south in the low levels. The maximum SLP anomaly gradient also coincides with the most southerly V850. A prominent Z500 ridge/trough pattern is evident with positive Z500 anomalies to the west and negative anomalies to the east of the coldest T850 anomalies. This is a common Z500 pattern for mid-latitude cold anomalies (Loikith and Broccoli 2012). Node 15 occurrences are most common from May through August, indicating that this is predominantly a cold winter pattern, similar to Node 22, and therefore may be of interest to impacts resulting from extreme cold.

Similar patterns can be connected across the SOM with areas of strong SLP anomaly gradients coinciding with the strongest T850 anomalies through promotion of deviations from the climatological westerlies. In cases where T850 anomalies are weak, SLP, Z500, and V250 anomalies are also weak, further supporting this synoptic connection between anomalies in atmospheric pressure and advection of anomalous temperature. These connections are also consistent across seasons.

In a similar fashion as for T850, Fig. 5 shows composites of daily precipitation accumulation for days assigned to each node. In general, nodes towards the top and right sides of the SOM are wetter than nodes towards the bottom and left sides. This coincides with LSMPs characterized by primarily negative SLP anomalies towards the top and right and positive SLP anomalies towards the bottom and left. For nodes with relatively high precipitation amounts, variability from node to node is mostly manifested in the northward extent of precipitation along the Pacific Coast and Andes Mountains with inter-node variability in precipitation also pronounced over northeastern Argentina and Uruguay.

To further diagnose the mechanisms leading to the precipitation patterns in Fig. 5, Fig. 6 shows composites of IVT and Fig. 7 shows the total number of days assigned to each node that were coincident with an AR at each grid point. The magenta contours in Fig. 6 highlight the 250 kg/m/s^2 value, which is a threshold commonly used to determine whether an atmospheric river (AR) is present (Gimeno et al. 2014). Here, this threshold outline is provided as reference indicating that the node mean IVT exceeds this fixed AR threshold (note that a different thresholding approach was used to objectively identify AR days in Fig. 7, as described in Sect. 2). There is a strong relationship between precipitation, IVT, and number of AR days across all nodes. Regions of relatively high precipitation mostly coincide with areas of elevated IVT and a relatively large number of AR days, while dry areas or dry nodes show a lack of ARs and low IVT values. This relationship is overall consistent with expectations, especially in that ARs are defined by anomalous IVT and generally associated with precipitation. However, together these results indicate that precipitation over much of southern South America is highly related to ARs, and that high values of IVT are most often associated with these narrow AR structures. In other words, ARs are a key contributor of precipitation in the region, especially along the Pacific Coast where orographic lifting is maximized.

In Fig. 5, Nodes 13, 14, 20, and 21 stand out as having the most extensive and heavy precipitation in the SOM. These nodes are also associated with relatively high IVT and a large number of AR days. Days assigned to these nodes tend to have a strong negative SLP anomaly, with the important difference across the four nodes being the location of the SLP anomaly center. The north side of the SLP anomaly center is characterized by a gradient that promotes low level onshore winds along the Pacific Coast and is associated with the axis of highest number of ARs and largest mean IVT values along with the most precipitation. When the AR associated with the mid-latitude storm intercepts and is lifted by the Andes Mountains, orographic precipitation enhancement leads to the relatively high precipitation values for these nodes. This effect is clearly illustrated in Nodes 13 and 14. In Node 13, the SLP anomaly center is farther south than in Node 14. This corresponds to the maximum precipitation, IVT, and AR count in Node 13 being south of the maxima in Node 14. This same relationship between the location of maximum precipitation, IVT, AR count, and SLP anomaly center is also evident in Nodes 20 and 21 with Node 21 showing the most northerly maxima.

The SOMs also depict upper level support for precipitation and the associated IVT and ARs for these nodes, and others with precipitation. Notable Z500 troughs are found upstream of these wet regions with some indication of the Z500 anomaly centers being slightly upstream of the negative SLP anomaly centers. At jet stream level, all four node patterns are associated with anomalously strong V250, providing further support for upward vertical motion and steering the storm track towards the Andes. This is most prominent for Node 14 where very strong positive V250 anomalies are coincident with the heaviest precipitation. These four nodes are also associated with strong temperature anomalies in Fig. 4, with warm anomalies ahead of the area of precipitation and cool behind, likely indicative of the presence of a cold front contributing to the precipitation, consistent with ARs often being associated with cold fronts

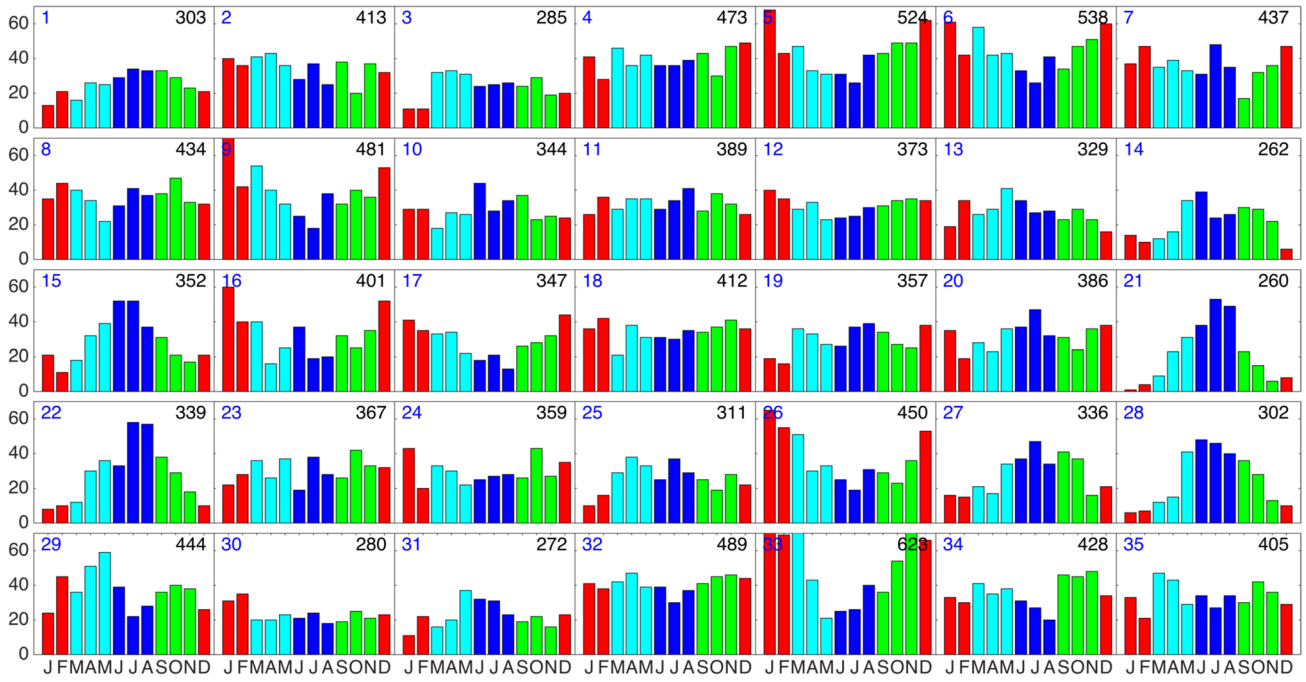

Fig. 3 Histograms of node occurrence frequency by month for each SOM node. The left most bar is for January and then follows the annual cycle to the right with the rightmost bar being for December. Red bars are for meteorological summer, cyan for fall, blue for winter, and green for spring. The blue numbers in the upper left are the node numbers and the black numbers in the upper right are the number of days in the entire 37-year climatology assigned to the node

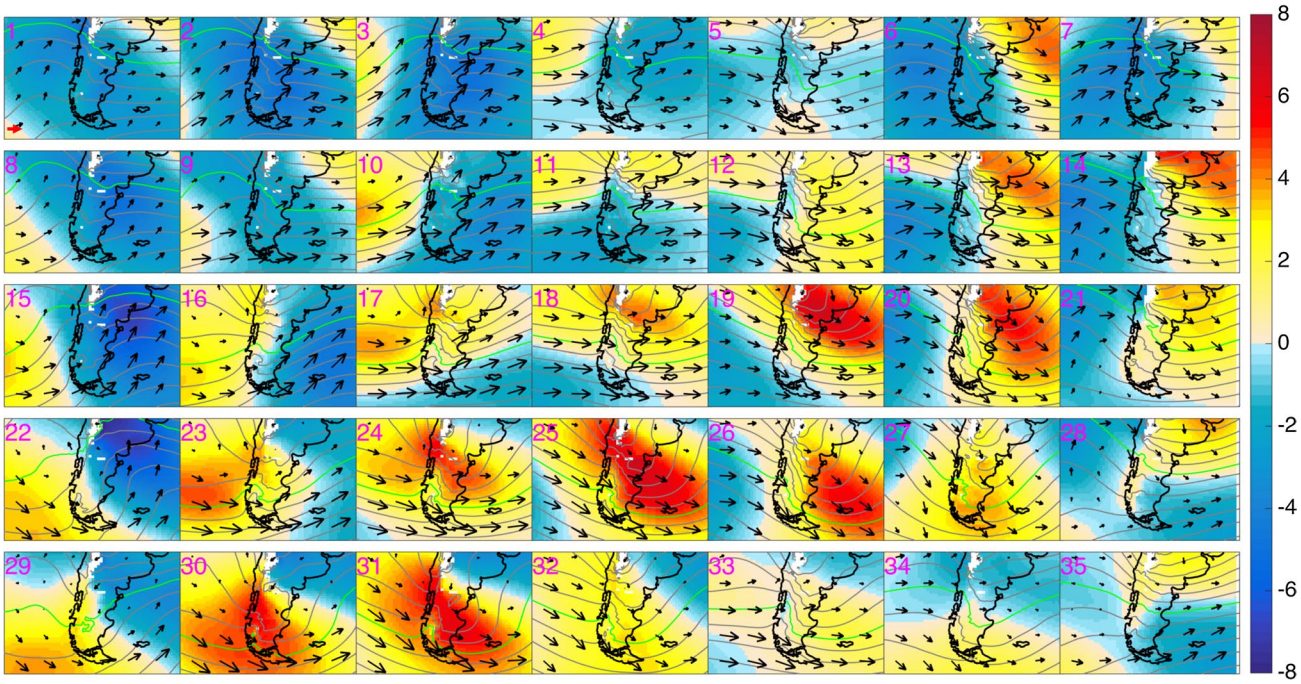

Fig. 4 Composites of 850 hPa temperature anomalies (shading in K), total field 850 hPa temperature (gray contours, every 2° K with the green contour the 3° line for reference), and total field 850 hPa wind speed and direction (arrows in m/s). The red arrow at the bottom left of the Node 1 panel is equal to 10 m/s. The numbers in the top left refer to the corresponding SOM nodes

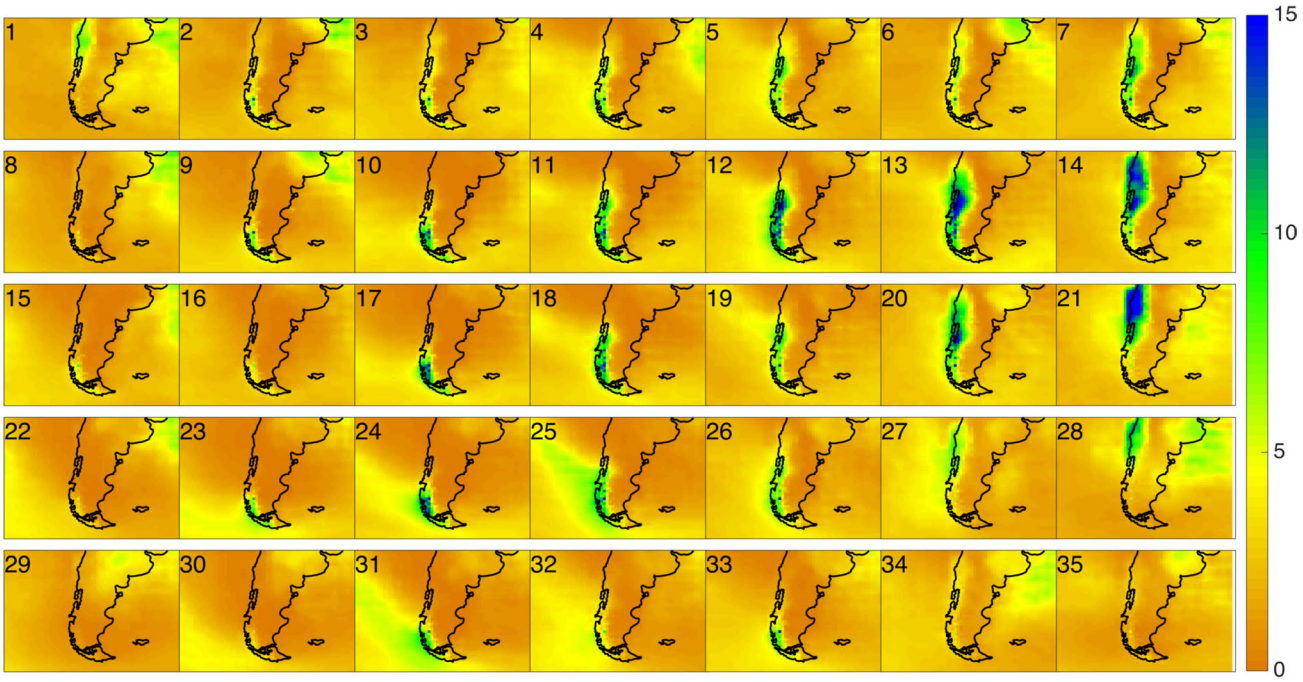

Fig. 5 Composites of daily precipitation rate (mm/day) for days assigned each of the 35 nodes. Numbers at the top left correspond to the SOM node numbers

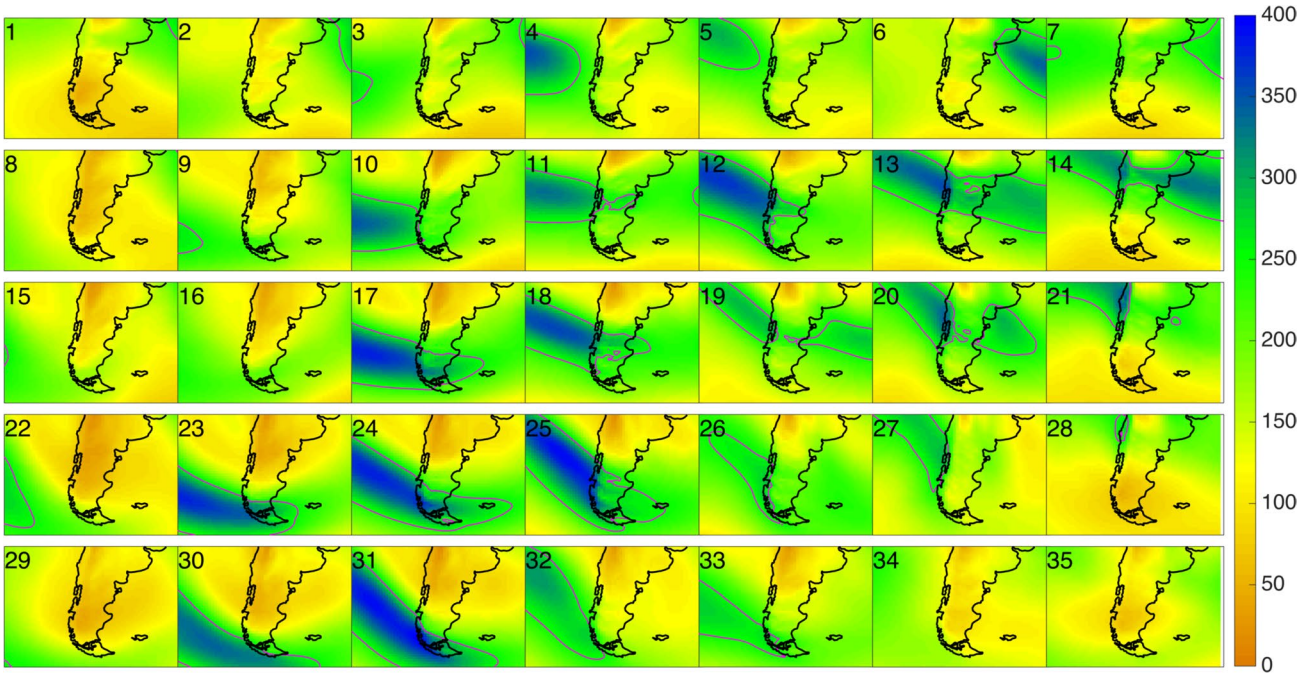

Fig. 6 Same as in Fig. 5 except for integrated water vapor transport in kg/m/s^2. Magenta contours correspond to the 250 kg/m/s^2 value, a common threshold for defining an atmospheric river

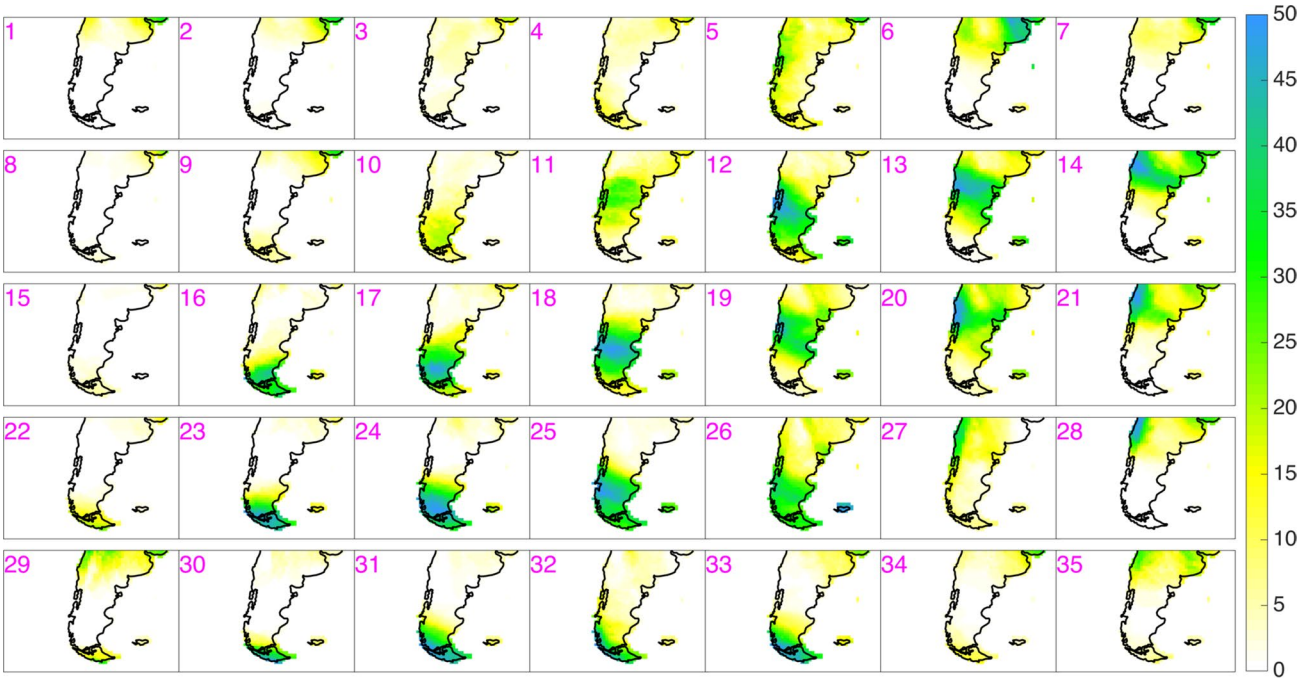

Fig. 7 Grid pointwise total number of atmospheric river days for days assigned to each node. Units are in days and only provided over land

in the mid-latitudes (Ralph et al. 2004; Dacre et al. 2015; Ryoo et al. 2015; Warner and Mass 2017).

The driest nodes generally show an opposite pattern to the wettest nodes. Nodes 8, 15, and 35 stand out as having relatively low amounts of precipitation across much of the domain with the exception of northern Argentina and Uruguay. While the synoptic setup for each of the three nodes differs somewhat, all three nodes share positive SLP anomalies and strong gradients that oppose the climatological westerlies. This reduces the transport of low-level moisture which can be lifted by the Andes resulting in little or no precipitation there. This is further supported by the very small number of AR days assigned to these nodes and the low values of IVT. At Z500, these dry patterns generally show an upstream ridge with relatively weak V250 anomalies indicating that the primary storm track is displaced away from the region and there is little or no support by the jet stream for storm development at the synoptic scale. Nodes 8 and 15 also coincide with anomalously cool temperatures (Fig. 4) as low-level winds advect cool and dry air northwards.

3.4 Interannual variability and association with climate modes

The stacked bar charts in Fig. 8 show the number of node assignments per year, plotted as the fraction of days, stratified by season. Each of the 35 nodes is assigned a color with the color shading scaling with pattern similarity rather than node number. This node order reassignment is accomplished using the following methodology. Starting with the Node 29 tri-variate LSMP at the bottom left corner of the SOM (Fig. 2), the pattern correlation is computed between it and the 34 other tri-variate LSMPs corresponding to the 34 other nodes. The nodes are then rearranged in order of decreasing similarity to Node 29 based on the pattern correlation coefficient. In other words, blue patterns tend to be on the bottom left of the SOM, getting more dissimilar to Node 29 as the blues fade to greens, while red patterns are the least similar to Node 29 and tend to be at the top right of the SOM. Node 29 is therefore most different from Node 13 and most similar to Node 30. While this reordering could begin at any node, Node 29 was chosen because it is clearly distinct from the other corners of the SOM.

Considerable interannual variability in node occurrence is clearly apparent across the seasonal cycle. For example, 2001 stands out with a highly anomalous DJF with a distinct predominance of days assigned to nodes near the upper right portion of the SOM (warm colors). This translates to a season dominated by anomalously low SLP, Z500 troughs, and anomalously strong V250. These patterns also tend to be anomalously wet across the Andes with many patterns being associated with high IVT values and AR day counts, suggesting an unusual number of days with patterns conducive to rainfall in some parts of the domain during summer 2001. In the other three seasons, DJF was not unusual in its distribution of node assignments indicating that this was a single season anomaly.

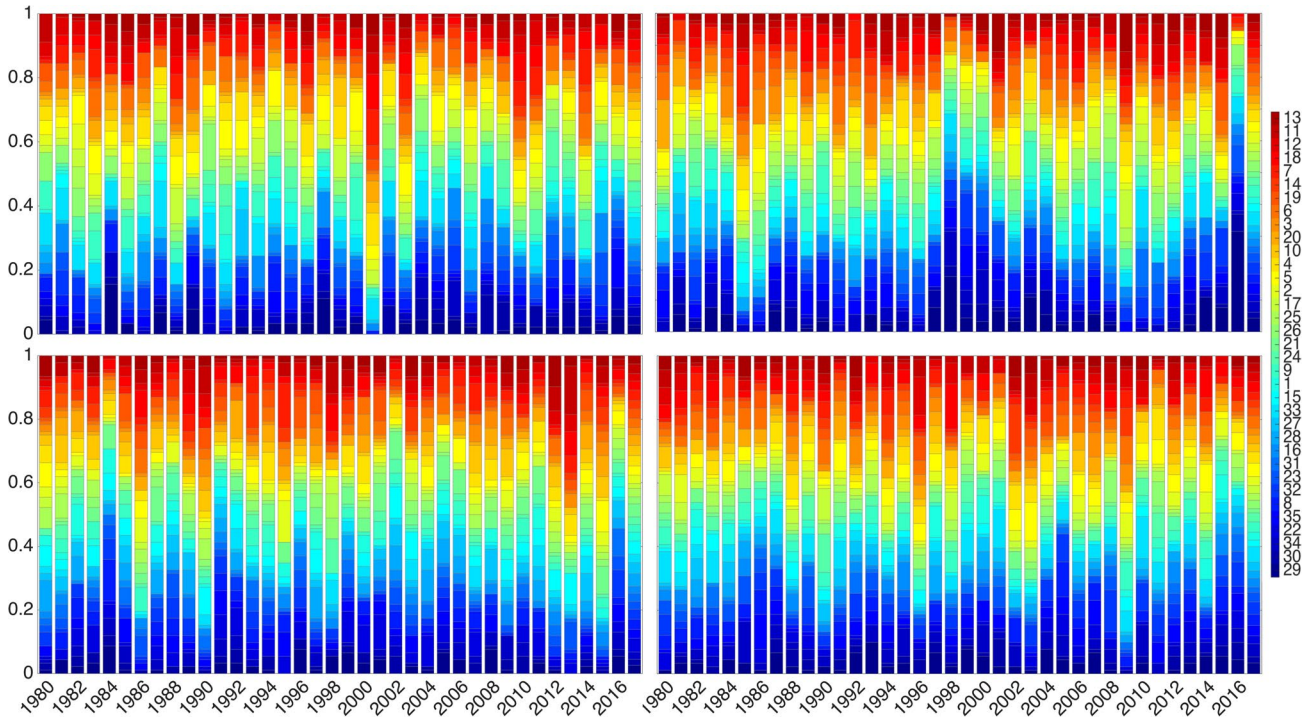

Fig. 8 Stacked bar charts showing the proportion of days in each year assigned to each node, stratified by season. Each node is assigned a color as indicated in color bar. Panels are for (top left) DJF, (top right) MAM, (bottom left) JJA, and (bottom right) SON. The rightmost bar shows the 37-year average occurrence per year for each node for the season. For DJF, the first year is 1981 to ensure 3-month coherency across season. Therefore DJF 1981 consists of December of 1980 and January and February 1981

On the other hand, 1998 and 2016 stand out as unusual for MAM with nodes located towards the bottom left of the SOM dominating. During 2016, roughly one third of all days were assigned to Node 29 and for both seasons very few days were assigned to patterns along the top right of the SOM. These nodes are generally dominated by positive SLP anomalies across the domain and especially across the southern portion of the domain, positive Z500 anomalies maximized across the southern half of the domain, and anomalously weak V250. The fact that these seasons were following the peak of a strong warm phase ENSO event (warm phase conditions were present from 2015 into 2016) suggests a likely influence of the event on the frequency of LSMP type for the season.

Figure 9 shows composites for each of the three SOM input variables for (left) days when the MEI was in its lowest quartile and (right) when the MEI was in its highest quartile. The upper quartile composites generally resemble the node patterns that were unusually common during the strong warm ENSO years of 1998 and 2016, supporting ENSO as an important influence on the distribution of node pattern frequency during MAM. Similar behavior, however, is not apparent following the warm phase of the very strong 1983 event in any season and the influence of cold phase events on interannual variability is not clearly evident in Fig. 8. The box plots in Fig. 10 shows the range of MEI values for days assigned to each of the 35 nodes, and could be interpreted as an association between ENSO and node frequency, stratified by each season. In MAM, the relationship between Nodes 27 and 29 is clearly evident and the corresponding patterns for both nodes visually resemble the top quartile MEI patterns in Fig. 9. For most other nodes across the season, there is only a modest relationship between ENSO and node assignment, with many nodes concurrent with a range of MEI values. There is some indication of a relationship between cold ENSO phases in DJF with Nodes 23, 24, 30, and 31 and the composites of SLP, Z500, and V250 for days in the lower quartile of the DJF MEI distribution closely resemble these node patterns (not shown).

Figure 11 shows the box plots of SAM values for days assigned to each of the 35 nodes, and reveals the relationship between each node and the SAM index, stratified by season. Compared with ENSO, the relationship between the SAM and node frequency is stronger and more consistent across the seasonal cycle, as evidenced by the greater number of nodes that show larger deviations from zero and have preferentially positive or negative index values. In general, the higher numbered nodes tend to be associated with a more positive SAM than the lower numbered nodes, indicating that node patterns towards the bottom of the SOM are more

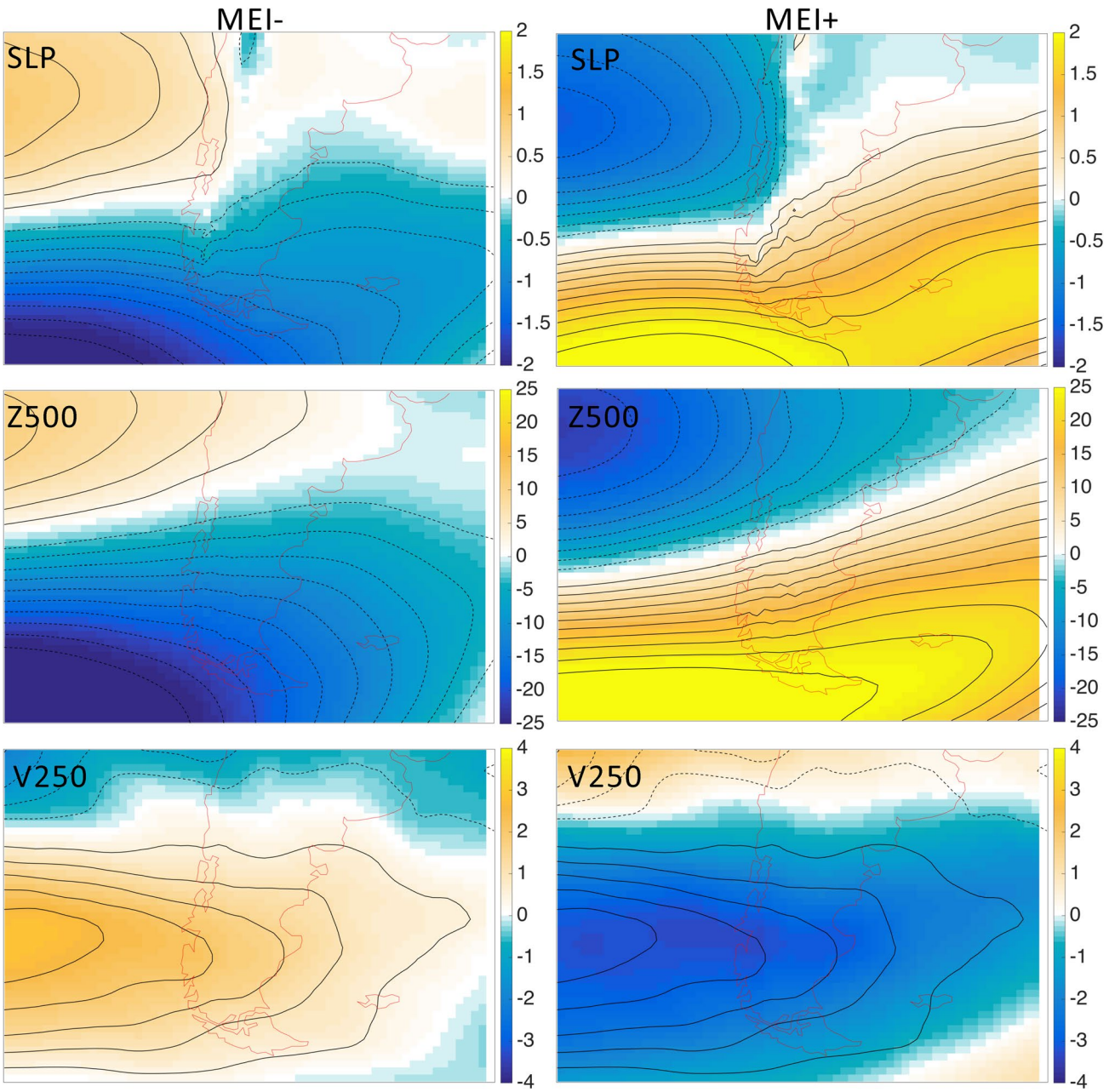

Fig. 9 Composites of (top) SLP in hPa, (middle) Z500 in m, and (bottom) V250 in m/s for days when the MEI was in the (left) lower and (right) upper quartiles of the index frequency distribution. Results are only for March, April, and May

associated with a positive SAM than node patterns at the top of the SOM. However, within each SOM row, additional SAM-node relationship variability is evident. Nodes 23, 30, and 31 stand out in all seasons as having a particularly strong association with a positive phase of the SAM. These node patterns are dominated by an area of positive SLP anomalies, a prominent Z500 ridge, and positive V250 anomalies on the southern edge of the region, indicative of a southward displacement of the jet stream and associated confinement of cooler air towards the pole. These patterns resemble composites of the three SOM input variables for days concurrent with the upper quartile of the SAM index distribution (Fig. 12). This indicates that the SOM is able to capture variability in LSMPs connected with this hemispheric mode of climate variability. This pattern also coincides with anomalously warm T850 over the southern half of the landmass, with cool anomalies along the northern third, consistent with previously documented SAM temperature associations (e.g. Garreaud et al. 2009). Furthermore, these node patterns are characterized by low amounts of precipitation across most of

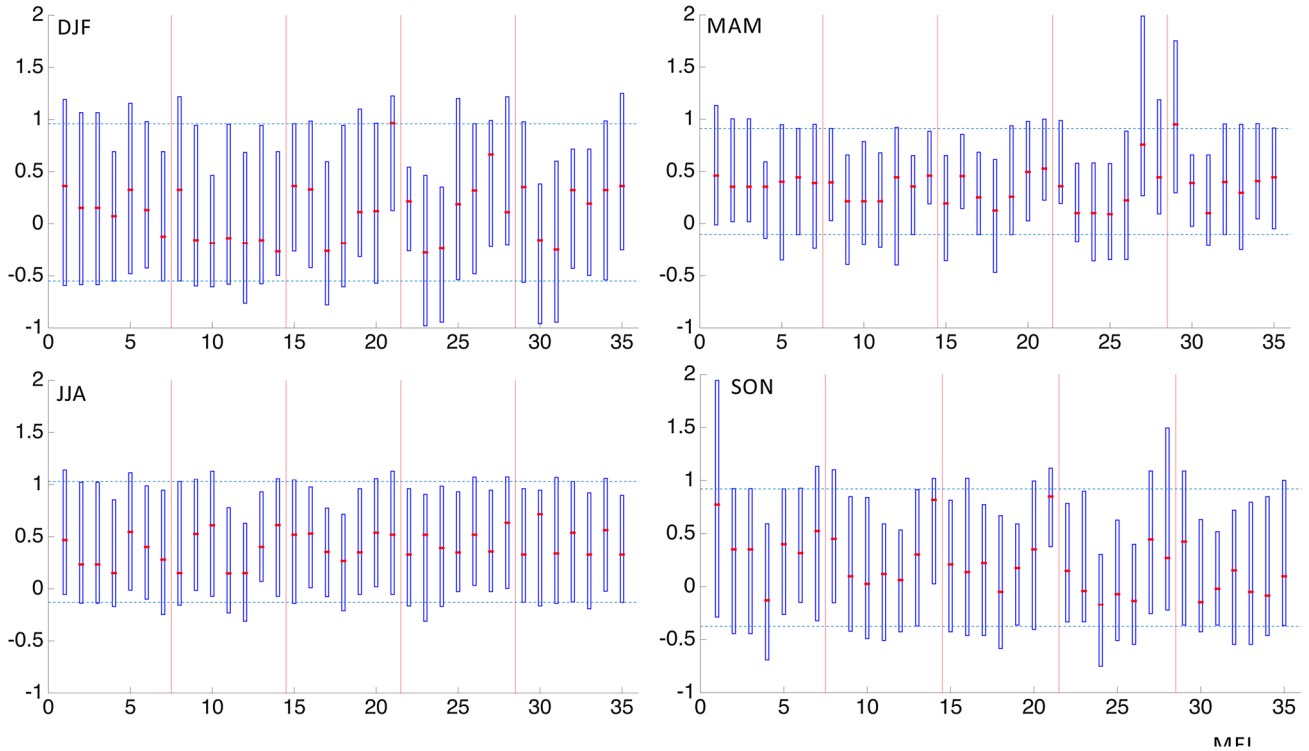

Fig. 10 Box plots showing the range of MEI values (*y* axis) for days assigned to each of the 35 nodes (*x* axis) stratified by season. Blue boxes show the 25th to 75th percentiles of the distribution of MEI values for each node and the red lines mark the median. Vertical red lines are placed every seven nodes to delineate horizontal rows (comprised of seven nodes in each row) in the SOM in Fig. 2. The bottom and top blue dashed horizontal lines show the 25th and 75th percentiles of the seasonal MEI distribution, respectively

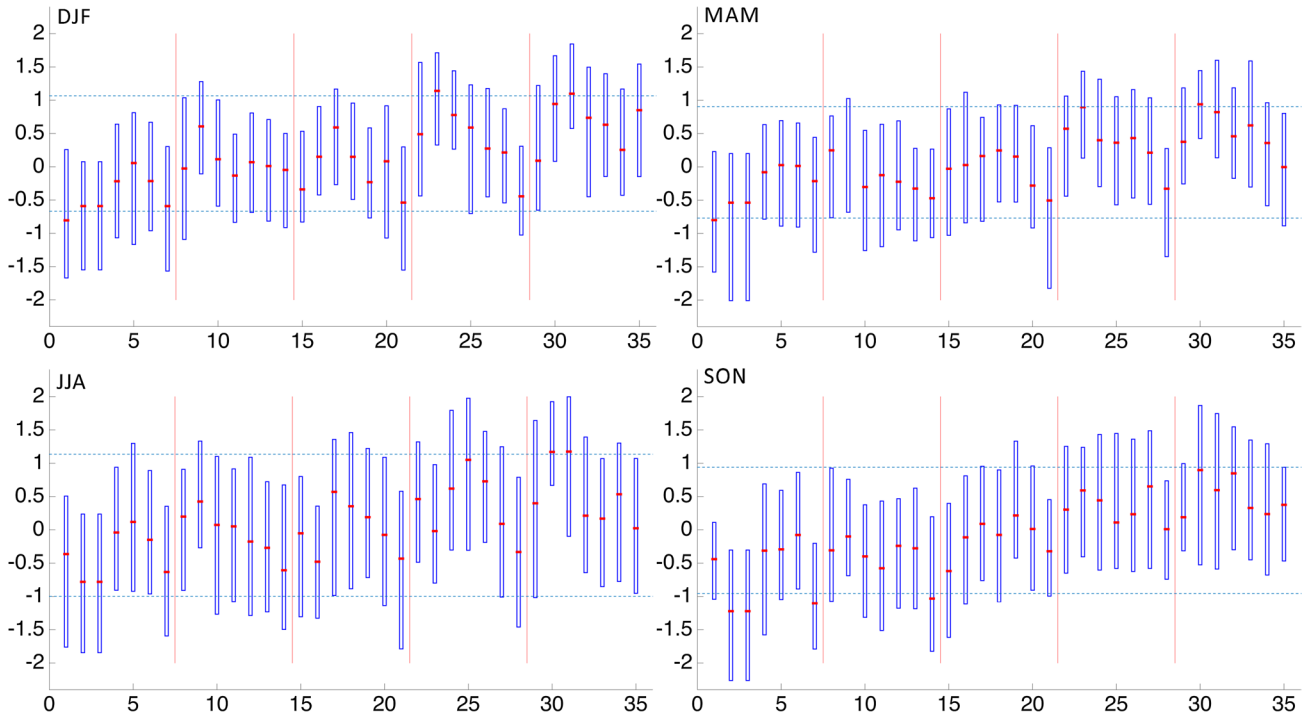

Fig. 11 Same as in Fig. 10 except for the SAM

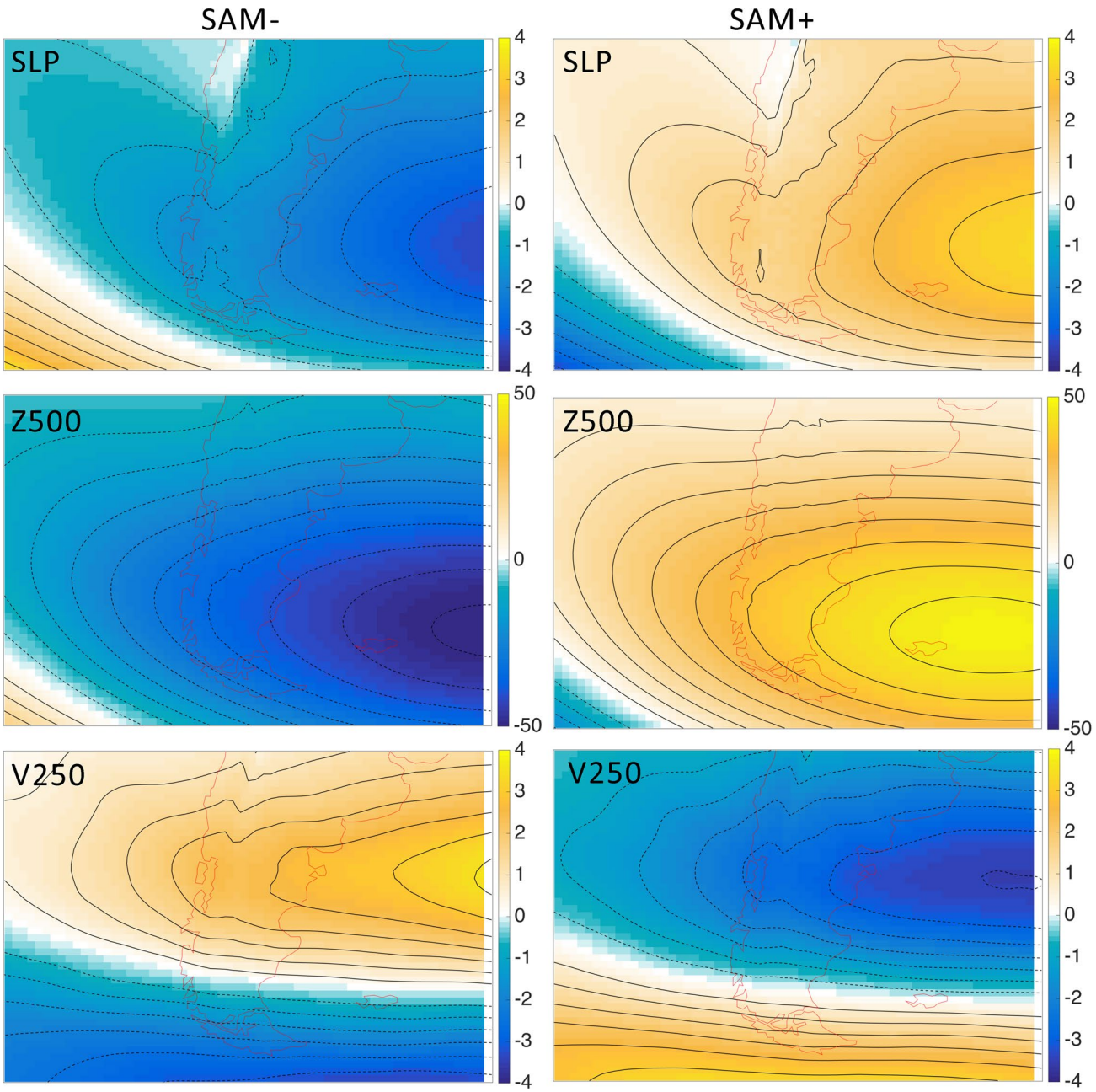

Fig. 12 Same as in Fig. 10 except for the SAM and for the entire year

the domain, consistent with the negative phase of the SAM being associated with a lower frequency of extratropical cyclone and frontal passages (Reboita et al. 2009).

For the negative phase of the SAM, Nodes 1, 2, and 3 show relatively strong associations in all seasons. Node 7 also shows a strong relationship for DJF and SON while Node 14 shows a strong relationship during SON, but not other seasons. Nodes 1 through 3 are characterized by a SLP anomaly gradient over much of the region, although that gradient goes from north to south in Node 1 and west to east in Nodes 2 and 3. At Z500, the region is primarily dominated by a trough, with a ridge to the south in Node 1 and to the west in Nodes 2 and 3. V250 anomalies are positive along the northern portion of the domain for Nodes 1 and 2, with a somewhat different pattern for Node 3. All three patterns are associated with negative T850 anomalies over most of the domain (Fig. 4), driven at the low levels by an anomalous equatorward trajectory in V850. The node patterns most associated with the negative phase of the SAM tend to resemble the composites of the SOM input variables for

days when the SAM is in its lowest quartile (Fig. 12). Some differences exist in the exact placement of the SLP, V250, and Z500 anomaly centers, which is to be expected since the node/SAM relationship is not absolute. However, this lends further support to the SOM approach effectively capturing the influence of important climate modes on LSMPs in southern South America.

4 Summary and conclusions

Southern South America experiences a wide range of large-scale meteorological patterns (LSMPs) in association with variability in several key surface meteorological variables and processes including temperature, wind, precipitation, and moisture transport. Self-organizing maps (SOMs) are used here to characterize the range of possible LSMP types over southern South America (Fig. 2). LSMPs are defined using three meteorologically important circulation variables, sea level pressure (SLP), 500 hPa geopotential height (Z500), and 250 hPa wind speed (V250). With every day in the 37-year record analyzed assigned to one of 35 SOM-defined clusters or "nodes", associations with other meteorological variables that are important for impacts can be connected with the driving LSMPs. Here we focus on lower tropospheric temperature and wind (Fig. 4) and precipitation (Fig. 5). Furthermore, additional insight into the physical drivers of these impacts can be inferred by connecting the LSMPs with meteorological mechanisms. Here we focus on integrated water vapor transport (IVT) and the related presence of atmospheric rivers (ARs; Figs. 6, 7). The frequency of occurrence of LSMP type exhibits considerable inter-seasonal and inter-annual variability (Fig. 8), with some of this variability in daily patterns showing association with the Southern Annular Mode (SAM), and the El Nino Southern Oscillation (ENSO; Figs. 9, 10, 11, 12).

The range of LSMPs over southern South America displayed by the SOM in Fig. 2 can be summarized as a spectrum from those largely dominated by positive SLP and Z500 anomalies concurrent with a poleward displacement of the 250 hPa jet stream winds, to a regime generally dominated by negative SLP and Z500 anomalies concurrent with an equatorward displacement of the 250 hPa jet stream winds. All three variables demonstrate importance in the occurrence of lower tropospheric temperature anomalies and precipitation. Anomalies in the SLP field and associated anomalies in low level winds result in anomalous meridional temperature advection based on the wind trajectories. This near-surface relationship is supported by Z500 ridges and troughs, coincident with warm and cold atmospheric temperature anomalies respectively with an approaching Z500 trough conducive to precipitation. The placement of the jet stream either poleward or equatorward of its climatological mean position indicates meridional excursions of anomalous warm and cold airmasses, respectively. Variability in the jet stream winds also correspond to precipitation via modulations of the mid-latitude storm track and associated upward vertical motion. Precipitation in the region is strongly related to AR occurrence, with wet nodes and wet regions associated with a high number of AR days and dry nodes and dry regions not associated with ARs. Therefore, ARs are a key driver of precipitation over the region, especially along the Pacific Coast and the west side of the Andes Mountains where orographic lift of the low level moisture in the AR can enhance precipitation rates.

While the plurality of variability across LSMPs cannot be explained by modulations of the phase and magnitude of the SAM and ENSO, amplified phases of both modes do show some influence on which LSMPs occur when. ENSO is demonstrated to be most influential during austral fall, while the SAM can influence LSMP frequency during all seasons. Loikith et al. (2017a, b) showed modest relationships between the SAM and extreme temperatures over this region, with weak relationships with ENSO, and speculated that synoptic scale variability likely played an important role in the occurrence of extremes. Results here, while not specifically focused on temperature extremes, lend support to the hypothesis that synoptic scale weather variability is key to driving climate impacts, such as extremes, apart from the influence of recurrent climate modes. However, the analysis in the present study only considers two modes of variability, in isolation, and concurrent relationships. Interaction between the SAM and ENSO could play some role (Fogt and Bromwich 2006) while other modes of variability shown to modulate ENSO impacts, namely the Pacific Decadal Oscillation, could have some influence on LSMP type occurrence (Kayano et al. 2011). Lastly, this study does not consider impacts from Atlantic Ocean sea surface temperature variability, which could play a small role in LSMP type variability (e.g. Knight et al. 2005, 2006).

The comprehensive synoptic climatology presented here helps further our understanding of the range of LSMPs that occur across southern South America and their influence on surface meteorology. The methodology presented is also extensible to other synoptically driven meteorological phenomena such as extremes or low level jets while the SOMs themselves could be constructed using other atmospheric fields of interest for particular applications. Further implications of these findings, while useful in the study of synoptic meteorology and climatology, provide potential for climate change analysis. Specifically, the LSMPs and their connections to other related meteorological fields could be assessed in climate model simulations of the historical past to better understand and help constrain model bias. Furthermore, quantification of whether climate models project systematic change in

LSMP frequency or character will help understand the skill with which drivers of change under global warming can be predicted.

Acknowledgements P. L., J. D., C. R. M., and A. B. acknowledge support from the U.S. National Science Foundation AGS-1547899. E. S. acknowledges support from the NASA Indicators for the National Climate Assessment (NCA) Program. Climate indices are obtained from the U.S. National Oceanic and Atmospheric Administration via the Web at https://www.esrl.noaa.gov/psd/data/climateindices/list/. MERRA2 reanalysis is available from the U.S. National Aeronautics and Space Administration via the Web at https://gmao.gsfc.nasa.gov/reanalysis/MERRA/. ERA-Interim data are available via the Web at https://www.ecmwf.int/en/research/climate-reanalysis/era-interim. University of Delaware data are available at https://www.esrl.noaa.gov/psd/data/gridded/data.UDel_AirT_Precip.html. We thank Hans Von Storch and Silvina Solman for their helpful contribution and guidance on this work. We thank Nathaniel Johnson for providing the SOMs Matlab code.

References

Andreoli RV, Kayano MT (2005) ENSO-related rainfall anomalies in South American and associate circulation features during warm and cold Pacific Decadal Oscillation regimes. Int J Climatol 25:2017–2030

Cassano EN, Glisan JM, Cassano JJ, Gutowski J, Seefeldt MW (2015) Self-organizing maps analysis of widespread temperature extremes in Alaska and Canada. Clim Res 62:199–218

Cassano JJ, Cassano EN, Seefeldt MW, Gutowski WJ, Glisan JM (2016) Synoptic conditions during wintertime temperature extremes in Alaska. J Geophys Res Atmos 121:3241–3262

Chen R, Lu R (2016) Role of large-scale circulation and terrain in causing extreme heat in western China. J. Clim 29:2511–2527

Chen HW, Alley RB, Zhang F (2016) Interannual Arctic sea ice variability and associated winter weather patterns: a regional perspective for 1979–2014. J Geophys Res Atmos 121:14433–14455. https://doi.org/10.1002/2016jd024769

Dacre HF, Clark PA, Martinez-Alvarado O, Stringer MA, Lavers DA (2015) How do atmospheric rivers form? Bull Am Meteorol Soc 96:1243–1255

DeAngeles AM, Broccoli AJ, Decker SG (2013) A comparison of CMIP3 simulations of precipitation over North America with observations: daily statistics and circulation features accompanying extreme events. J Clim 26:3209–3230

Fogt RL, Bromwich DH (2006) Decadal variability of the ENSO teleconnection to the high-latitude South Pacific governed by coupling with the southern annular mode. J Clim 19:979–997

Ford TW, Schoof JT (2016) Characterizing extreme and oppressive heat waves in Illinois. J Geophys Res Atmos 121:3326–3338. https://doi.org/10.1002/2016jd025721

Garreaud RD, Vuille M, Compagnucci R, Marengo J (2009) Present-day South American climate. Palaeogeogr Palaeoclimatol Palaeoecol 281:180–195

Geirinhas JL, Trigo RM, Libonati R, Coelho CAS, Palmeira AC (2018) Climatic and synoptic characterization of heat waves in Brazil. Int J Climatol 38:1760–1776

Gelaro R et al (2017) The modern-era retrospective analysis for research and applications, version 2 (MERRA-2). J Clim 30:5419–5454

Gervais M, Atallah E, Gyakum JR, Tremblay LB (2016) Arctic air masses in a warming world. J Clim 29:2359–2373

Gibson PB, Perkins-Kirkpatrick SE, Uotila P, Pepler AS, Alexander LV (2017) On the use of self-organizing maps for studying climate extremes. J Geophys Res Atmos 122:3891–3903

Gillett NP, Kell TD, Jones PD (2006) Regional climate impacts of the Southern Annular Mode. Geophys Res Lett 33:L23704

Gimeno L, Nieto R, Vázquez M, Lavers DA (2014) Atmospheric rivers: a mini-review. Front Earth Sci 2:2.1–2.6

Gimeno L, Dominguez F, Nieto R, Trigo R, Drumond A, Reason CJC, Taschetto AS, Ramos AM, Kumar R, Marengo J (2016) Major mechanisms of atmospheric moisture transport and their role in extreme precipitation. Annu Rev Environ Resour 41:117–141

Glisan JM, Gutowski WJ, Cassano JJ, Cassano EN, Seefeldt MW (2016) Analysis of WRF extreme daily precipitation over Alaska using self-organizing maps. J Geophys Res Atmos 121:7746–7761

Grimm AM, Tedeschi RG (2009) ENSO and extreme rainfall events in South America. J Clim 22:1589–1609

Grimm AM, Barros VR, Doyle ME (2000) Climate variability in southern South America associated with El Nino and La Nina events. J Clim 13:35–58

Grotjahn R, Lee Y-Y (2016) On climate model simulations of the large-scale meteorology associated with California heat waves. J Geophys Res Atmos 121:18–32

Grotjahn R et al (2016) North American extreme temperature events and related large scale meteorological patterns: a review of statistical methods, dynamics, modeling, and trends. Clim Dyn 46:1151–1184

Guan B, Waliser DE (2015) Detection of atmospheric rivers: Evaluation and application of an algorithm for global studies. J Geophys Res Atmos 120:12514–12535. https://doi.org/10.1002/2015JD024257

Guan B, Waliser DE, Ralph FM (2018) An intercomparison between reanalysis and dropsonde observations of the total water vapor transport in individual atmospheric rivers. J Hydrometeorol 19:321–337. https://doi.org/10.1175/JHM-D-17-0114.1

Hewitson BC, Crane RG (2002) Self-organizing maps: applications to synoptic climatology. Clim Res 22:13–26

Johnson NC, Feldstein SB (2010) The continuum of North Pacific sea level pressure patterns: intraseasonal, interannual, and interdecadal variability. J Clim 23:851–867

Johnson NC, Feldstein SB, Tremblay B (2008) The continuum of Northern Hemisphere teleconnection patterns and a description of the NAO shift with the use of self-organizing maps. J Clim 21:6354–6371

Kawazoe S, Gutowski WJ (2013) Regional very heavy daily precipitation in NARCCAP simulations. J Hydrometeorol 14:1212–1227

Kayano MT, Andreoli RV, De Souza RAF (2011) Evolving anomalous SST patterns leading to ENSO extremes. Relations between the tropical Pacific and Atlantic Oceans and the influence on the South American rainfall. Int J Climatol 31:1119–1134

Kayano MT, Andreoli RV, de Souza RAF, Garcia SR (2017) Spatiotemporal variability modes of surface air temperature in South America during the 1951–2010 period: ENSO and non-ENSO components. Int J Climatol 37:1–13

Knight JR, Allen RJ, Folland CK, Vellinga M, Mann ME (2005) A signature of persistent natural thermohaline circulation cycles in observed climate. Geophys Res Lett 32:L20708

Knight JR, Folland CK, Scaife AA (2006) Climate impacts of the Atlantic Multidecadal Oscillation. Geophys Res Lett 33:L17706

Krueger O, Hegerl GC, Tett SFB (2015) Evaluation of mechanisms of hot and cold days in climate models over Central Europe. Environ Res Lett 10:014002

Lau N-C, Nath MJ (2012) A model study of heat waves over North America: meteorological aspects and projections for the twenty-first century. J Clim 25:4761–4784

Lavers DA, Villarini G, Allan RP, Wood EF, Wade AJ (2012) The detection of atmospheric rivers in atmospheric reanalyses and their

links to British winter floods and the large-scale climatic circulation. J Geophys Res 117:D20106. https://doi.org/10.1029/2012JD018027
Lee Y-Y, Gotjahn R (2016) California Central Valley summer heat waves from two ways. J Clim 29:1201–1217
Lennard C, Hegerl G (2015) Relating changes in synoptic circulation to the surface rainfall response using self-organising maps. Clim Dyn 44:861–879
Loikith PC, Broccoli AJ (2012) Characteristics of observed atmospheric circulation patterns associated with temperature extremes over North America. J Clim 25:7266–7281
Loikith PC, Broccoli AJ (2015) Comparison between observed and model-simulated atmospheric circulation patterns associated with extreme temperature days over North America using CMIP5 historical simulations. J Clim 28:2063–2079
Loikith PC, Waliser DE, Lee H, Neelin JD, Lintner B, McGinnis S, Mearns L, Kim J (2015) Evaluation of large-scale meteorological patterns associated with temperature extremes in the NARCCAP regional climate model simulations. Clim Dyn 45:3257–3274
Loikith PC, Lintner B, Sweeney A (2017a) Characterizing large-scale meteorological patterns and associated temperature and precipitation extremes over the northwestern United States using self-organizing maps. J Clim 30:2829–2847
Loikith PC, Detzer J, Mechoso CR, Lee H, Barkhordarian A (2017b) The influence of recurrent modes of climate variability on the occurrence of monthly temperature extremes over South America. J Geophys Res Atmos. https://doi.org/10.1002/2017JD027561
Muñoz ÁG, Goddard L, Robertson AW, Kushnir Y, Baethgen W (2015) Cross-time scale interactions and rainfall extreme events in southeastern South America for the austral summer. Part I: potential predictors. J Clim 28:7894–7913
Neiman PJ, Ralph FM, Wick GA, Lundquist JD, Dettinger MD (2008) Meteorological characteristics and overland precipitation impacts of atmospheric rivers affecting the West Coast of North America based on eight years of SSM/I satellite observations. J Hydrometeorol 9:22–47. https://doi.org/10.1175/2007JHM855.1
Pezza AB, van Rensch P, Cai W (2012) Severe heat waves in Southern Australia: synoptic climatology and large scale connections. Clim Dyn 38:209–224
Radic V, Cannon AJ, Menounos B, Nayeob G (2015) Future changes in autumn atmospheric river events in British Columbia, Canada, as projected CMIP global climate models. J Geophys Res Atmos 120:9279–9302
Ralph FM, Neiman PJ, Wick GA (2004) Satellite and CALJET aircraft observations of atmospheric rivers over the eastern North Pacific Ocean during the winter of 1997/98. Mon Weather Rev 132:1721–1745
Reboita MS, Ambrizzi T, Porfírio da Rocha R (2009) Relationship between the southern annular mode and southern hemisphere atmospheric systems. Rev Bras Meteorol 24:48–55
Reichle RH et al (2018) Land surface precipitation in MERRA-2. J Clim 30:1643–1664
Renom M, Rusticucci M, Barreiro M (2011) Multidecadal changes in the relationship between extreme temperature events in Uruguay and the general atmospheric circulation. Clim Dyn 37:2471–2480
Ryoo J-M, Waliser DE, Waugh DW, Wong S, Fetzer EJ, Fung I (2015) Classification of atmospheric river events on the U.S. West Coast using a trajectory model. J Geophys Res Atmos 120:3007–3028
Sheridan SC, Lee CC (2011) The self-organizing map in synoptic climatological research. Prog Phys Geogr 35:109–119
Silvestri G, Vera C (2009) Nonstationary impacts of the southern annular mode on southern hemisphere climate. J Clim 22:6142–6148
Solman SA, Menendez CG (2003) Weather regimes in the South American sector and neighbouring oceans during winter. Clim Dyn 21:91–104
Thompson DWJ, Wallace JM (2000) Annular modes in the extratropical circulation. Part I: month-to-month variability. J Clim 13:1000–1016
Viale M, Valenzuela R, Garreaud RD, Ralph MF (2018) Impacts of atmospheric rivers on precipitation in southern South America. J Hydrometeorol 19:1671–1687
Waliser D, Guan B (2017) Extreme winds and precipitation during landfall of atmospheric rivers. Nat Geosci 10:179–183
Warner MD, Mass CF (2017) Changes in climatology, structure, and seasonality of northeast Pacific atmospheric rivers in CMIP5 climate simulations. J Hydrometeorol 18:2131–2141
Wolter K, Timlin MS (1998) Measuring the strength of ENSO events: how does 1997/1998 rank? Weather 53:315–324
Xie Z, Black RX, Deng Y (2017) The structure and large-scale organization of extreme cold waves over the conterminous United States. Clim Dyn 49:4075–4088
Zhu Y, Newell RE (1998) A proposed algorithm for moisture fluxes from atmospheric rivers. Mon Weather Rev 126:725–735